Multidimensional screening yields channelrhodopsin variants having improved photocurrent and order-of-magnitude reductions in calcium and proton currents

Yong Ku Cho, Demian Park*, Aimei Yang*, Fei Chen, Amy S. Chuong, Nathan C. Klapoetke, Edward S. Boyden

MIT Media Lab and McGovern Institute, Departments of Biological Engineering and Brain and Cognitive Sciences, MIT, Cambridge, Massachusetts 02139

To whom correspondence should be addressed: Edward S. Boyden, Departments of Biological Engineering and Brain and Cognitive Sciences, MIT Media Lab and McGovern Institute, Building E15: E15-485, 20 Ames St., Cambridge, MA 02139; Phone: 617-324-3085; Fax: 617-253-6285; E-mail: esb@media.mit.edu. *, equal contribution.

Supplementary Results

Reversal potential measurements for ChR2 mutants characterized using patch clamp

We first measured the reversal potentials of peak and steady-state components of the 10 point mutants electrophysiologically characterized, downstream of the calcium and proton selectivity stage (**Fig. 4d, e**) for sodium (**Supp. Fig. 2a**), calcium (**Supp. Fig. 2b**), and protons (**Supp. Fig. 2c**) (see **Methods** for composition of solutions). The H114G mutant showed a positive shift in sodium reversal potential (**Supp. Fig. 2a**), consistent with the increase in sodium photocurrent for H114G (**Supp. Fig. 4a**). Many mutants identified in the screen had both decreases in calcium photocurrent (**Supp. Fig. 4b**) and decreases in calcium reversal potential (**Supp. Fig. 2b**). A similar trend held for protons (**Supp. Fig. 4c**; **Supp. Fig. 2c**). We calculated a measure of relative selectivity, calcium reversal potential minus that of sodium (**Supp. Fig. 2d**), and found statistically significant shifts of this value ranging from -10 mV to -25 mV relative to wild type for most of the mutants. Similarly, half of the mutants had downward shifts in proton reversal potential minus sodium reversal potential (**Supp. Fig. 2e**). The differences between photocurrent measurements (**Fig. 4d, e**) and reversal potential measurements may be explained by the fact that calcium- and proton- binding sites, as well as potential interactions between multiple ions, may differentially affect photocurrents driven from baseline vs. reversal potential (see refs. (1-7), and discussion below about complications using the Goldman-Hodgkin-Katz equation to interpret reversal potentials).

Correlated effects of mutations on calcium and proton permeability as determined by reversal potential measurements

As noted in the main text, there is a correlation between the photocurrents of calcium vs. proton (each divided by that of sodium) (**Supp. Fig. 3a, b**) for the 10 point mutants electrophysiologically characterized downstream of the calcium and proton selectivity stage. We also noted a significant correlation in reversal potential measurements for calcium vs. proton (each subtracting off that of sodium) for both peak ($r(9) = 0.77$, $P < 0.01$, Pearson's correlation coefficient; **Supp. Fig. 3c**) and steady-state ($r(9) = 0.90$, $P < 0.001$, Pearson's correlation coefficient, **Supp. Fig. 3d**) components.

Reversal potential measurements for ChR2 mutant combinations

We measured reversal potentials of ChR2 mutant combinations (double mutants A71S/E90A, E90A/H114G, ChromeT, and ChromeQ), for sodium (**Supp. Fig. 6a**), calcium (**Supp. Fig. 6b**), and protons (**Supp. Fig. 6c**), obtaining strong shifts in calcium and proton reversal potential for all of the mutants assessed, for both the peak and steady state components, and ~35 mV shifts in calcium reversal potential and ~45 mv shifts in proton reversal potential for ChromeQ. When we compared relative selectivity, namely calcium reversal potential minus that of sodium (**Supp. Fig. 6d**) and proton reversal potential minus that of sodium (**Supp. Fig. 6e**), strong shifts again were again observed.

Permeability ratios estimated from reversal potential measurements

Channels that transport multiple kinds of ion, and that might possess multiple binding sites, are biophysically complex to model (5-7). Channelrhodopsins may potentially possess such properties (1-4,8), with four different native ionic species capable of passing through, and the potentiality of one or more binding sites for one or more ions. Accordingly, we have focused on analyzing both peak as well as steady-state ion specific photocurrents (**Fig. 4d, 4e, 5**). Other papers have attempted to estimate channelrhodopsin ion permeabilities using the Goldman-Hodgkin-Katz (GHK) equation (9), but it also has been controversial about whether the GHK can be used, even in modified form (1), since the assumption of independent movement of different ionic species in the GHK equation may not hold true for channelrhodopsins, potentially due to the complexities named above (2-4). Complicating matters further is the fact that no single channel conductances have been measured for any channelrhodopsin, due to their small values, meaning that many key parameters are not known. Thus, we estimate ion permeabilities as in ref. (1) for completeness, with the acknowledgment that while they reflect one potential interpretation of the reversal potential measurements, they may only provide a rough estimate, which we denote P^* in **Supp. Fig. 7**. The wild-type ChR2 has permeability ratio of calcium vs. sodium of ~0.20, and of proton vs. sodium of ~690,000. The estimated permeability ratios for the 10 point mutants electrophysiologically characterized downstream of the calcium and proton selectivity stage, as well as the combinatorial mutants, were generally lower than that of the wild-type, and for the combinatorial mutants, greatly lower – ChromeQ, for example, had a permeability ratio of calcium vs. sodium of 0.048 and a permeability ratio of proton vs. sodium of 91,000. Thus, while acknowledging that these are estimates, the results are consistent with our photocurrent data.

Additional characterization of ChromeT and ChromeQ

When we compared the photocurrent density of ChromeT and ChromeQ in Tyrode's solution divided by the channelrhodopsin expression level (as indicated by the brightness of the fused fluorophore), compared to that of wild-type ChR2, there was a 3-fold increase for the peak component (n = 6-10 HEK293FT cells, $P < 0.05$ t-test comparing peak photocurrent density divided by the total fluorescence, to that of wild-type ChR2; **Supp. Fig. 8a**) and 5-fold increase in the steady-state component (n = 6-10 HEK293FT cells, $P < 0.01$ t-test comparing peak photocurrent density divided by the total fluorescence, to that of wild-type ChR2; **Supp. Fig. 8a**). Although this measure may reflect other factors such as altered membrane trafficking and protein folding efficiency, it suggests that the effective conductance of ChromeT and ChromeQ may be significantly higher than that of wild-type ChR2.

In addition, when we measured the potassium photocurrent (**Supp. Fig. 8b**), the potassium-to-sodium photocurrent ratios of ChromeT and ChromeQ were not significantly changed compared to wild-type ChR2, suggesting that the selectivity for potassium over sodium was not significantly altered (n = 6-7 HEK293FT cells, $P > 0.8$ t-test comparing I_potassium/I_sodium to that of wild-type ChR2; **Supp. Fig. 8c**).

Extracted voltage measurement vs. Fura-2 ratio or SNARF-5F ratio of ChR2 variants

To aid the identification of ChR2 variants with high extracted voltage measurement (EVM) but reduced calcium or proton flux, we generated additional figures, in which the EVM of ChR2 variants is plotted on the x-axis, and Fura-2 ratio or SNARF-5F ratio after illumination is plotted on the y-axis (**Supp. Fig. 9**). Indicated in red are the residues we identified earlier as resulting in significantly reduced calcium flux (**Supp. Fig. 9a,** mutants with reduced Fura-2 ratio in **Fig. 4bi**) or proton flux (**Supp. Fig. 9b**, mutants with reduced SNARF-5F in **Fig. 4bii**), when mutated to specific new residues, as compared to wild-type ChR2**.** We focused on identifying variants with reduced calcium flux or proton flux compared to WT ChR2, which is a stringent condition considering that they were screened first for improved EVM. A less stringent, but more comprehensive approach would be to find variants with reduced calcium flux/EVM ratio (**Supp. Fig. 9a**). To compare the calcium flux/EVM ratios across mutants, we divided the Fura-2 ratio (**Fig. 4bi**) by the EVM (**Fig. 3a**), and performed a statistical comparison of this ratio vs. wild-type. Since this is a ratio of two variables, we calculated the standard deviation using the same formula used for comparing photocurrent ratios (see **Experimental Procedures**). When we compared the calcium flux/EVM ratios, mutations I84L, E90A, F98M and H134R had significantly smaller calcium flux/EVM ratio than the wild-type (**Supp. Fig. 9a;** indicated in blue are new variants found from this analysis, indicated in red are mutations with reduced Fura-2 ratio identified from **Fig. 4bi**, Bonferroni-corrected t-test comparing Fura-2 ratio/EVM to that of wild-type). When we compared the proton flux/EVM ratio, mutations E90A, M91L, F98M, A111L, L132C, H134K, and H134R had significantly smaller values than the wild-type (**Supp. Fig. 9b**; indicated in blue are new variants found from this analysis, indicated in red are mutations with reduced SNARF-5F ratio identified from **Fig. 4bii**, Bonferroni-corrected t-test comparing SNARF-5 ratio/EVM to that of wild-type). For enhanced ion selectivity, it may be beneficial to add these mutations to the ChromeQ mutant (for which we chose mutations not based upon the analysis of **Supp. Fig 9**, but through the methods described in the main text). We measured the photocurrent of mutants F98M, A111L, and H134K using whole-cell patch clamp in HEK293FT cells (**Fig. 3d-g**). In this analysis, the peak and steady-state photocurrents of F98M were not significantly different from that of WT ChR2 (**Fig. 3d, e**), but the steady-state/peak photocurrent ratio was greater than that of WT ChR2 (**Fig. 3f**). The channel closing rate was similar to WT ChR2 (**Fig. 3g**). In the future, it may be useful to add this mutation to ChromeQ to see if there is further reduction in calcium flux. As for mutants A111L and H134K, they showed significantly higher photocurrents than the WT (**Fig. 3d, e**; only steady-state for A111L, both peak and steady-state for H134K), but the channel closing rate was significantly slower than the WT (**Fig. 3g**). As for L132C and H134R, previous reports have shown that they have significantly slower channel closing rates (10,11), so if added to ChromeQ, mutations A111L, L132C, H134K, and H134R may reduce the performance in driving repetitive spikes in neurons.

Supplementary Experimental Procedures

In order to measure reversal potentials, liquid junction potentials were determined for each intracellular-extracellular solution pair as previously described (12). Using the intracellular solutions in the methods, the liquid junction potentials were 5.8 mV, and 4.9 mV, for 90mM $CaCl_2$ and 135 mM NMDG, respectively, and were corrected during recording; the others were < 1 mV in liquid junction potential. Reversal potential for each mutant was determined by first measuring photocurrents at holding potentials between -80 to + 80 mV in 20 mV steps to get a rough estimate, and then in 5 mV steps near the reversal potential, which allowed linear fits (typical $R^2 = 0.98$). Reversal potentials were calculated from equations for the linear fits in Excel (Microsoft). In order to calculate reversal potential for the steady-state photocurrents, photocurrents were averaged over the final 300 ms of a 1 s illumination. The standard deviations for the subtraction of two reversal potentials were calculated using the following formula:

$$Var[X - Y] = Var[X] + Var[Y]$$

In order to estimate permeability ratios, the reversal potential measurements were fitted to a modified Goldman-Hodgkin-Katz equation with a correction for divalent cations (13) as has been done previously for ChR2(1) using MATLAB.

Supplementary Figures

Supplementary Figure 1. Results from the residue map stage of the screen in **Fig. 1a**. (a) Histograms of extracted voltage measurements (normalized to wild-type ChR2), of wild-type ChR2 (red) and site-saturation mutation libraries (blue) of indicated amino acid positions (n = 88-194 HEK293FT cells each; histograms normalized to peak). Gray box highlights two amino acid positions (D253 and K257) whose mutants show undetectable light-driven cell depolarization. (b) Extracted voltage measurements (normalized to that of wild-type ChR2) for site-saturation mutation libraries of amino acid positions 2-299 (n = 86 – 223 cells each). Filled bars, residues with normalized mean > 1 and $P < 0.05$, Bonferroni corrected Kolmogorov-Smirnov (K-S) test against wild-type ChR2; open bars, residues with normalized mean < 1 or $P > 0.05$, Bonferroni corrected Kolmogorov-Smirnov (K-S) test against wild-type ChR2; gray highlighting, putative transmembrane domains estimated by alignment to a published crystal structure of a chimera between ChR1 and ChR2 (8). (c) Pre-Bonferroni corrected K-S test p-values for the site-saturation mutation libraries in (b).

Supplementary Figure 2. Reversal potential measurements for ChR2 mutants with improved ion selectivity. (a-c) Population data for reversal potentials, measured using whole-cell patch clamp in HEK cells in ion-specific extracellular solutions (see **Methods** for details), with peak (filled bars) and steady-state (open bars) reversal potentials, for wild-type ChR2 and the 10 ion selectivity mutants shown in **Fig. 4d, e**, for: sodium (E_rev_sodium) measured in 145 mM NaCl, pH 7.4 (a), calcium (E_rev_calcium) measured in 90 mM $CaCl_2$, pH 7.4 (b), and proton (E_rev_proton) measured in 135 mM NMDG, pH 6.4 (c) (n = 3-6 HEK293FT cells each). Plotted is mean and error bars representing standard error (S.E.). Dots indicate data from individual cells. (d-e) Population data for peak (filled bars) and steady-state (open bars) reversal potentials, relative to sodium reversal (n = 3-6 HEK293FT cells each), for: calcium

(E_rev_calcium – E_rev_sodium) (d), and proton (E_rev_proton – E_rev_sodium) (e). Illumination conditions: 470 nm, 1 s, 10 mW/mm^2 in all panels. Indicated are peak (dashed lines) and steady-state (dotted lines) reversal potentials for wild-type ChR2. Statistics for all panels: *, $P < 0.05$; **, $P < 0.01$, ***, $P < 0.001$, non-Bonferroni corrected t-test comparing mutant vs. wild-type.

Supplementary Figure 3. Correlation between calcium and proton selectivity in ChR2 mutants. (a, b) I_proton/I_sodium vs. I_calcium/I_sodium for both peak (a) and steady-state (b) photocurrents, for wild-type ChR2 and the 10 mutants with improved ion selectivity shown in **Fig. 4d, e** (n = 5-12 HEK293FT cells each). (c, d) E_rev_proton – E_rev_sodium vs. E_rev_calcium – E_rev_sodium, for both peak (c) and steady-state (d) photocurrents, for wild-type ChR2 and the 10 mutants in (a) and (b). Lines are linear regression fits.

Supplementary Figure 4. Photocurrent density of ChR2 mutants in ion-selective solutions. (a-c) Population data for peak (filled bars) and steady-state (open bars) photocurrent densities, measured using whole-cell patch clamp in HEK cells in ion-specific extracellular solutions (see **Methods** for details), for wild-type ChR2 and 10 mutants with improved ion selectivity shown in **Fig. 4d, e**, for: sodium (I_sodium) measured in 145 mM NaCl, pH 7.4 (a), calcium (I_calcium) measured in 90 mM $CaCl_2$, pH 7.4 (b), and proton (I_proton) measured in 135 mM NMDG, pH 6.4 (c) (n = 5-12 HEK293FT cells each). Plotted is mean and error bars representing S.E. Open circles indicate data from individual cells. Illumination conditions: 470 nm, 1 s, 10 mW/mm^2 in all panels. Indicated are peak (dashed lines) and steady-state (dotted lines) photocurrent densities for wild-type ChR2. Statistics for all panels: *, $P < 0.05$; **, $P < 0.01$, ***, $P < 0.001$, non-Bonferroni corrected t-test comparing mutant vs. wild-type.

Supplementary Figure 5. Ion selectivity of ChR2 mutant combinations assessed using photocurrent ratios. (a-c) Population data for peak (filled bars) and steady-state (open bars) photocurrent densities, measured using whole-cell patch clamp in HEK cells in ion-specific extracellular solutions (see **Methods** for details), for wild-type ChR2 and mutant combinations shown in **Fig. 5a** (n = 5-12 HEK293FT cells each), for: sodium (I_sodium) measured in 145 mM NaCl, pH 7.4 (a), calcium (I_calcium) measured in 90 mM $CaCl_2$, pH 7.4 (b), and proton (I_proton) measured in 135 mM NMDG, pH 6.4 (c). (d-e) Population data for peak (filled bars) and steady-state (open bars) photocurrent density ratios, measured using whole-cell patch clamp in HEK cells in ion-specific extracellular solutions, for wild-type ChR2 and mutant combinations shown in (a-c) (n = 5-12 HEK293FT cells each), for: calcium photocurrent (I_calcium) divided by sodium photocurrent (I_sodium) (d), and proton photocurrent (I_proton) divided by sodium photocurrent (I_sodium) (e). Illumination conditions: 470 nm, 1 s, 10 mW/mm^2 in all panels. Plotted is mean and error bars representing S.E. Open circles indicate data from individual cells. Indicated are peak (dashed lines) and steady-state (dotted lines) photocurrent densities (panels a, b, and c) and photocurrent ratios (panels d and e) for wild-type ChR2. Statistics for all panels: *, $P < 0.05$; **, $P < 0.01$, ***, $P < 0.001$, non-Bonferroni corrected t-test comparing mutant vs. wild-type.

Supplementary Figure 6. Reversal potential measurements for ChR2 mutant combinations. (a-c) Population data for peak (filled bars) and steady-state (open bars) reversal potentials, measured using whole-cell patch clamp in HEK cells in ion-specific extracellular solutions (see **Methods** for details), for wild-type ChR2 and mutant combinations shown in **Fig. 5a**, for: sodium (E_rev_sodium) measured in 145 mM NaCl, pH 7.4 (a), calcium (E_rev_calcium) measured in 90 mM $CaCl_2$, pH 7.4 (b), and proton (E_rev_proton) measured in 135 mM NMDG, pH 6.4 (c) (n = 3-8 HEK293FT cells each). (d-e) Population data for peak (filled bars) and steady-state (open bars) reversal potentials, relative to sodium reversal, for ChR2 mutant combinations shown in (a-c) (n = 3-8 HEK293FT cells each), for: calcium (E_rev_calcium – E_rev_sodium) (d), and proton (E_rev_proton – E_rev_sodium) (e). Illumination conditions: 470 nm, 1 s, 10 mW/mm^2 in all panels. Plotted is mean and error bars representing S.E. Open circles indicate data from individual cells. Indicated are peak (dashed lines) and steady-state (dotted lines) reversal potentials for wild-type ChR2. Statistics for all panels: *, $P < 0.05$; **, $P < 0.01$, ***, $P < 0.001$, non-Bonferroni corrected t-test comparing mutant vs. wild-type.

Supplementary Figure 7. Permeability ratios estimated from reversal potential measurements. (a-b) Estimated permeability ratios, calculated using a modified Goldman-Hodgkin-Katz equation (but see **Supplementary Results** for a discussion of why they may not be accurate), between calcium and -sodium (P*_calcium/P*_sodium) (a), and between protons and sodium (P*_proton/P*_sodium) (b), for ChR2, and mutants thereof.

Supplementary Figure 8. Characterization of ChromeT and ChromeQ photocurrent density and potassium conductance. (a) Population data for peak (filled bars) and steady-state (open bars) photocurrent density measured in Tyrode's solution divided by the total fluorescence (of fluorescent protein attached to the opsin) of each cell, of wild-type ChR2, ChromeT, and ChromeQ using 470 nm, 1 s illumination, 10 mW/mm^2 irradiance (n = 7-10 HEK293FT cells each). (b-c) Population data for peak (filled bars) and steady-state (open bars) potassium photocurrent properties measured using illumination conditions as in (a), including density measured in 145 mM KCl, pH 7.4 (b), as well as peak (filled bars) and steady-state (open bars) potassium photocurrent (I_potassium) divided by sodium photocurrent (I_sodium) (c), of wild-type ChR2, ChromeT, and ChromeQ (n = 6 HEK293FT cells each). Plotted is mean and error bars representing S.E. Open circles indicate data from individual cells. Statistics for all panels: *, $P < 0.05$; **, $P < 0.01$, ***, $P < 0.001$, non-Bonferroni corrected t-test comparing mutant vs. wild-type.

Supplementary Figure 9. Extended analysis to identify mutants with reduced calcium or proton flux, compared to extracted voltage measurement (EVM). (a) EVM (**Fig. 3a**) vs. Fura-2 ratio after illumination (**Fig. 4bi**). Indicated in blue are new variants found from comparing Fura-2 ratio/EVM (Bonferroni-corrected t-test comparing Fura-2 ratio/EVM to that of wild-type), indicated in red are mutations with reduced Fura-2 ratio identified from **Fig. 4bi.** (b) EVM (**Fig. 3a**) vs. SNARF-5F ratio after illumination (**Fig. 4bii**). Indicated in blue are new variants found from comparing SNARF-5F ratio/EVM (Bonferroni-

corrected t-test comparing SNARF-5F ratio/EVM to that of wild-type), indicated in red are mutations with reduced proton flux identified in **Fig. 4bii**. Plotted is mean and error bars representing S.E.

REFERENCES

1. Lin, J. Y., Lin, M. Z., Steinbach, P., and Tsien, R. Y. (2009) Characterization of engineered channelrhodopsin variants with improved properties and kinetics. *Biophys J* 96, 1803-1814
2. Berndt, A., Prigge, M., Gradmann, D., and Hegemann, P. (2010) Two open states with progressive proton selectivities in the branched channelrhodopsin-2 photocycle. *Biophys J* 98, 753-761
3. Gradmann, D., Berndt, A., Schneider, F., and Hegemann, P. (2011) Rectification of the channelrhodopsin early conductance. *Biophys J* 101, 1057-1068
4. Schneider, F., Gradmann, D., and Hegemann, P. (2013) Ion selectivity and competition in channelrhodopsins. *Biophys J* 105, 91-100
5. Eisenman, G., and Dani, J. A. (1987) An introduction to molecular architecture and permeability of ion channels. *Annu Rev Biophys Biophys Chem* 16, 205-226
6. Hess, P., Lansman, J. B., and Tsien, R. W. (1986) Calcium channel selectivity for divalent and monovalent cations. Voltage and concentration dependence of single channel current in ventricular heart cells. *J Gen Physiol* 88, 293-319
7. Eisenman, G., and Horn, R. (1983) Ionic selectivity revisited: the role of kinetic and equilibrium processes in ion permeation through channels. *J Membr Biol* 76, 197-225
8. Kato, H. E., Zhang, F., Yizhar, O., Ramakrishnan, C., Nishizawa, T., Hirata, K., Ito, J., Aita, Y., Tsukazaki, T., Hayashi, S., Hegemann, P., Maturana, A. D., Ishitani, R., Deisseroth, K., and Nureki, O. (2012) Crystal structure of the channelrhodopsin light-gated cation channel. *Nature* 482, 369-374
9. Nagel, G., Szellas, T., Huhn, W., Kateriya, S., Adeishvili, N., Berthold, P., Ollig, D., Hegemann, P., and Bamberg, E. (2003) Channelrhodopsin-2, a directly light-gated cation-selective membrane channel. *Proc Natl Acad Sci U S A* 100, 13940-13945
10. Lin, J. Y. (2011) A user's guide to channelrhodopsin variants: features, limitations and future developments. *Exp Physiol* 96, 19-25
11. Kleinlogel, S., Feldbauer, K., Dempski, R. E., Fotis, H., Wood, P. G., Bamann, C., and Bamberg, E. (2011) Ultra light-sensitive and fast neuronal activation with the Ca(2)+-permeable channelrhodopsin CatCh. *Nat Neurosci* 14, 513-518
12. Neher, E. (1992) Correction for liquid junction potentials in patch clamp experiments. *Methods Enzymol* 207, 123-131
13. Chang, D. C. (1983) Dependence of cellular potential on ionic concentrations. Data supporting a modification of the constant field equation. *Biophys J* 43, 149-156

Supplementary Figure-1 (Boyden)

a

representative results from the residue map screen
using voltage-sensitive FRET imaging, focused on identifying residues
with potential for yielding interesting point mutations

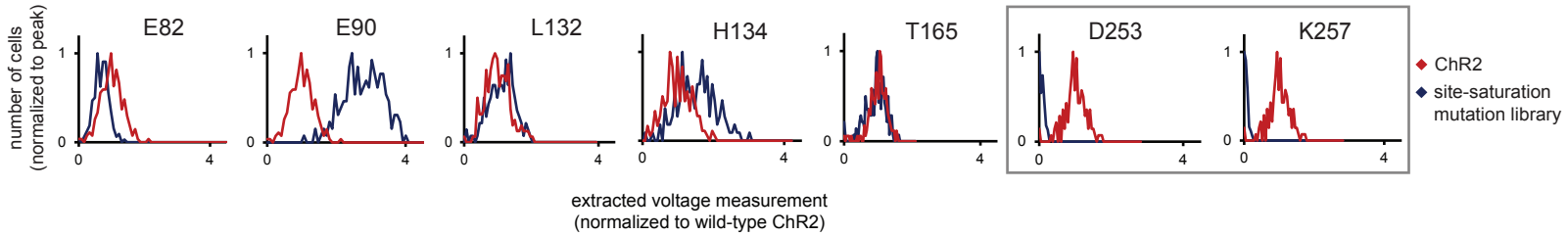

b

extracted voltage measurement of site-saturation mutation libraries at each amino acid postion

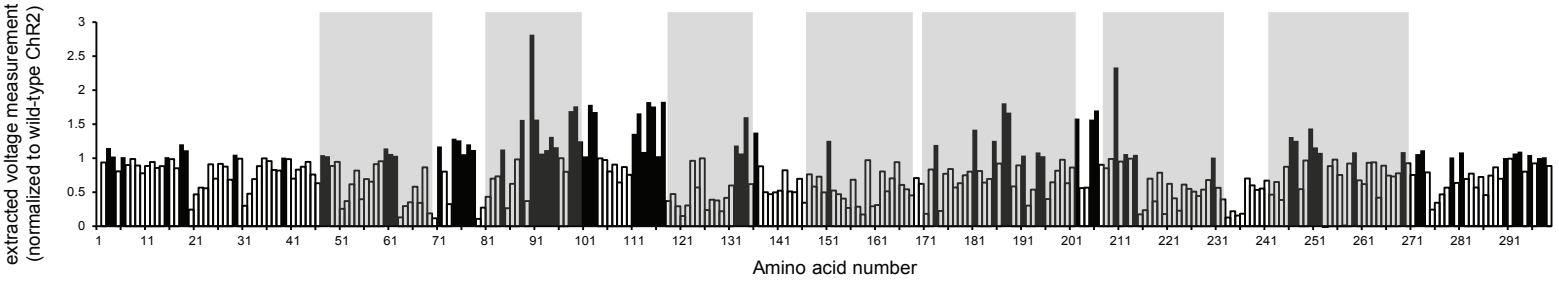

c

P-values of extracted voltage measurement, site-saturation mutation library vs. wild-type

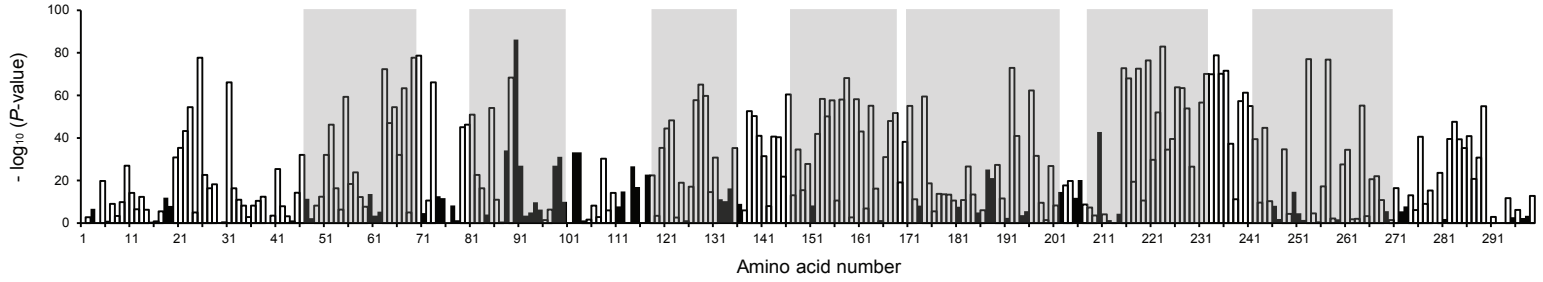

Supplementary Figure-2 (Boyden)

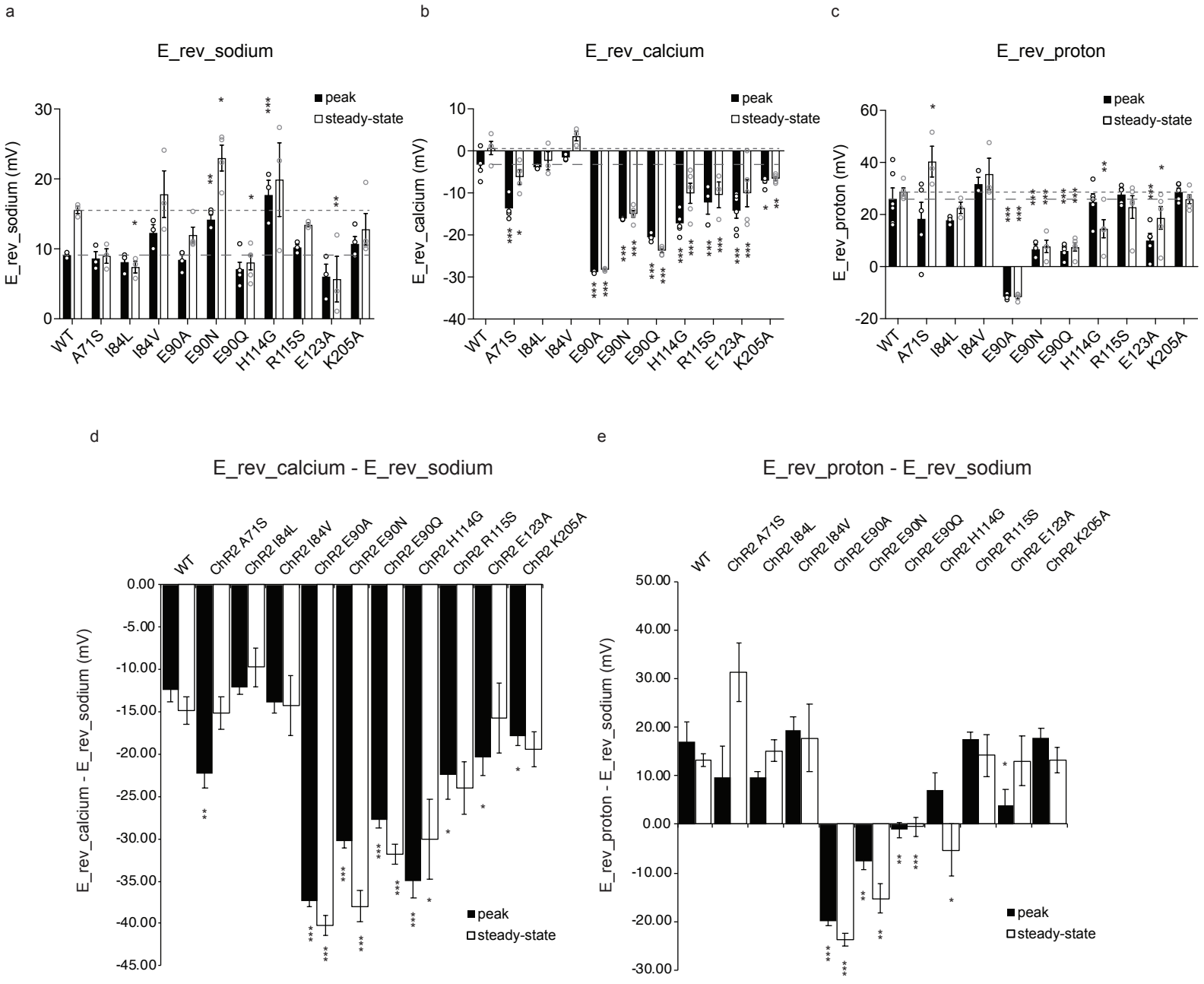

Supplementary Figure-3 (Boyden)

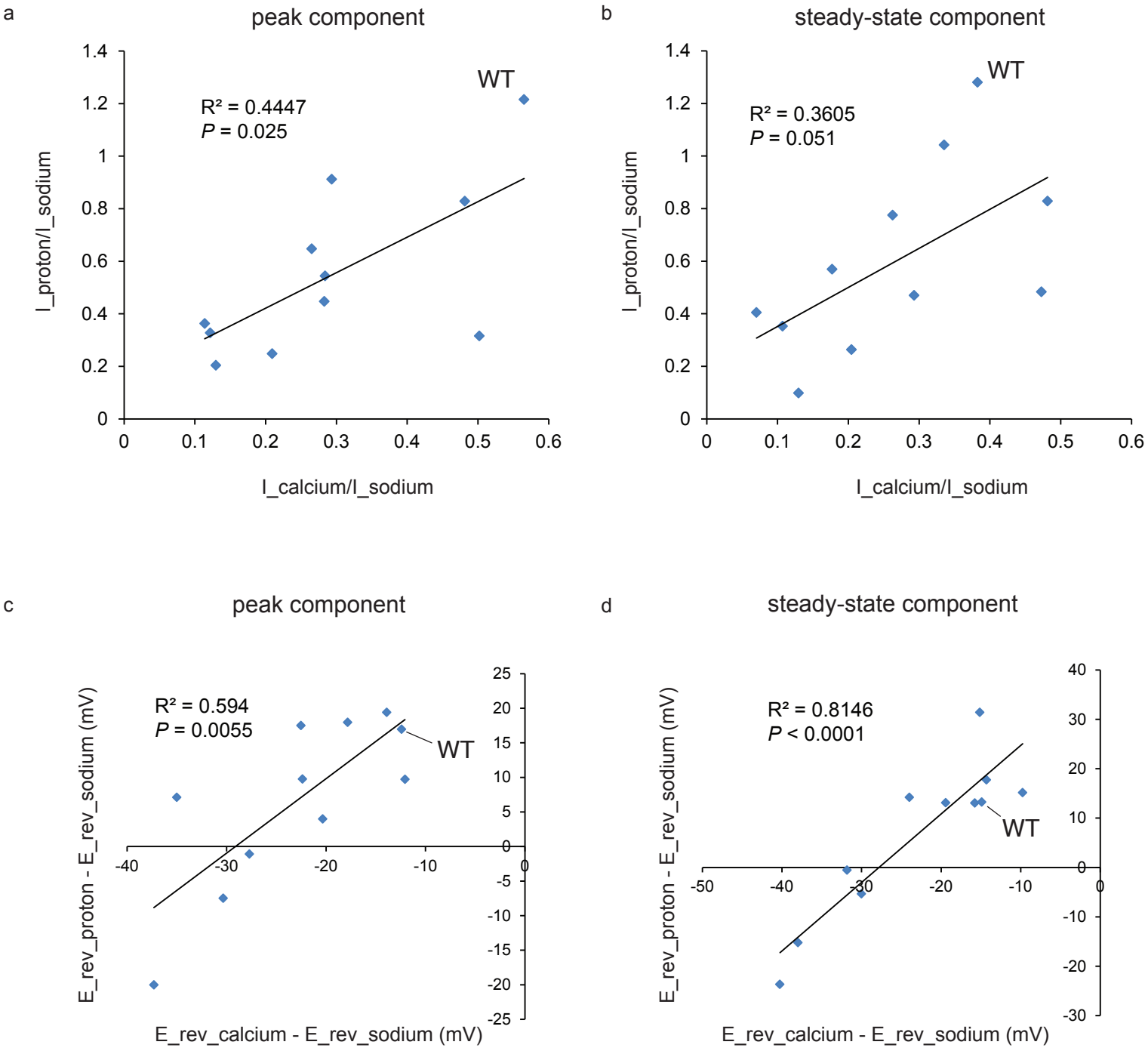

Supplementary Figure-4 (Boyden)

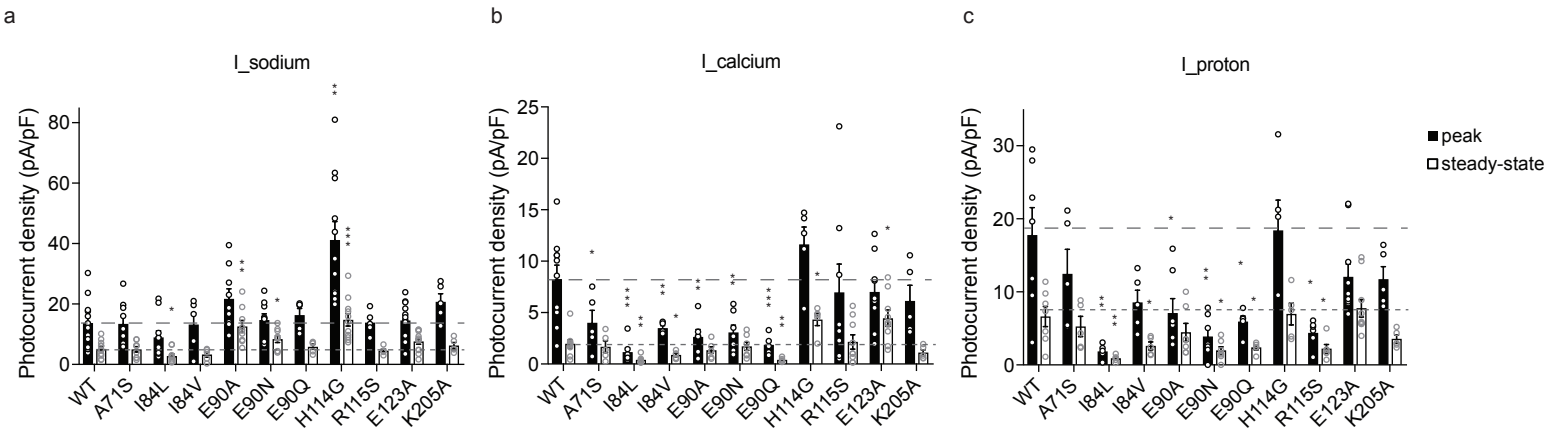

Supplementary Figure-5 (Boyden)

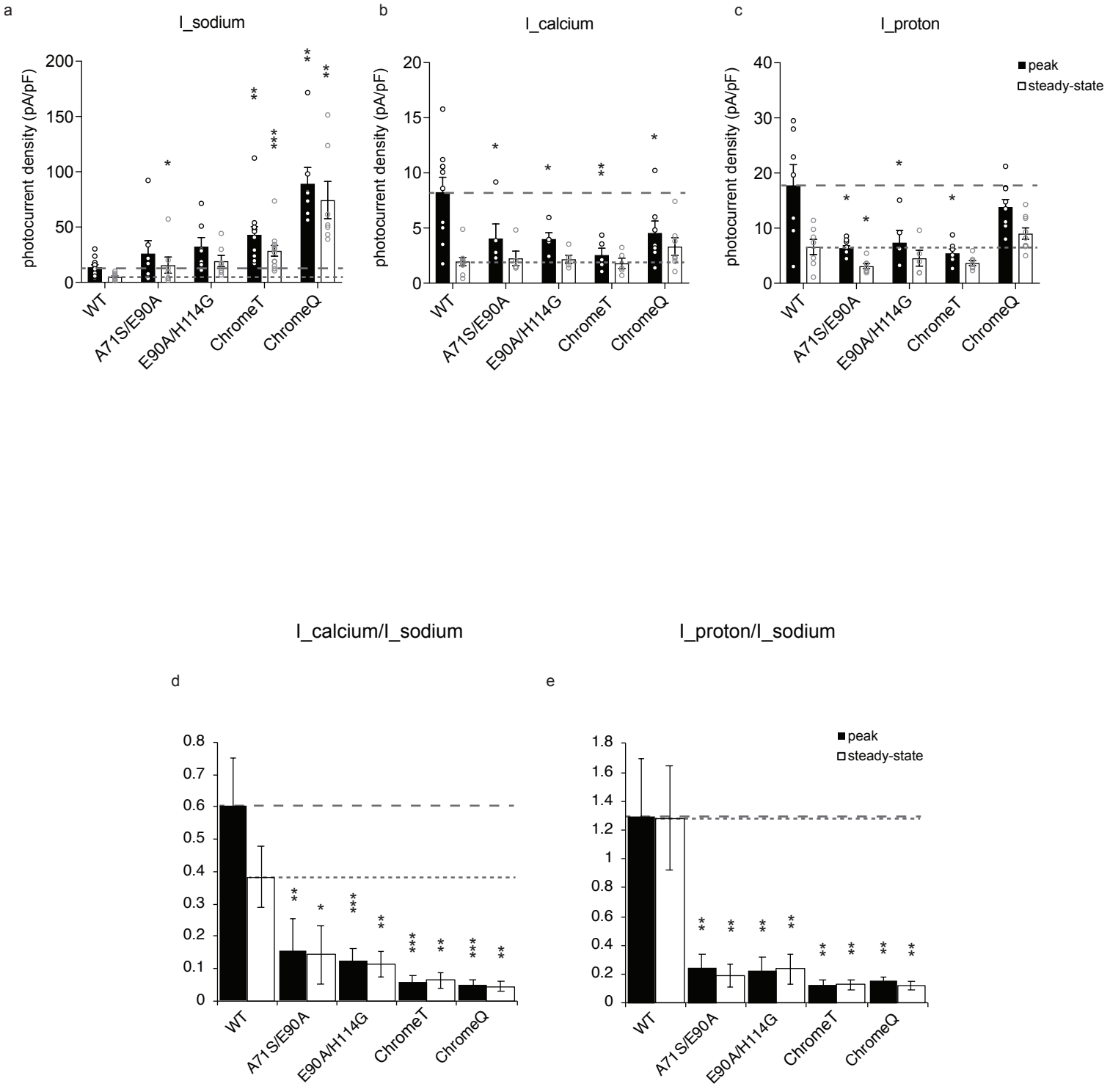

Supplementary Figure-6 (Boyden)

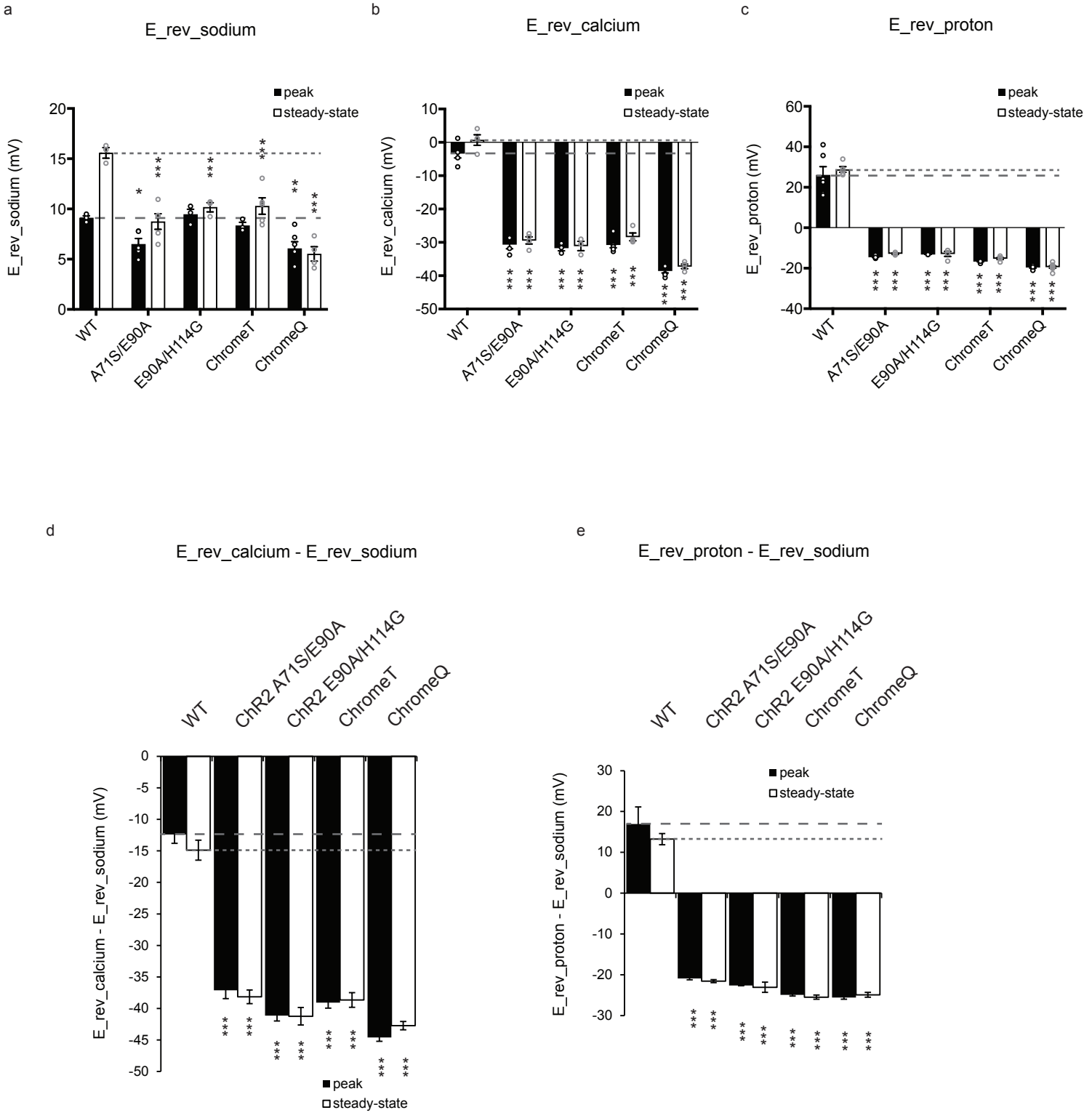

Supplementary Figure-7 (Boyden)

a

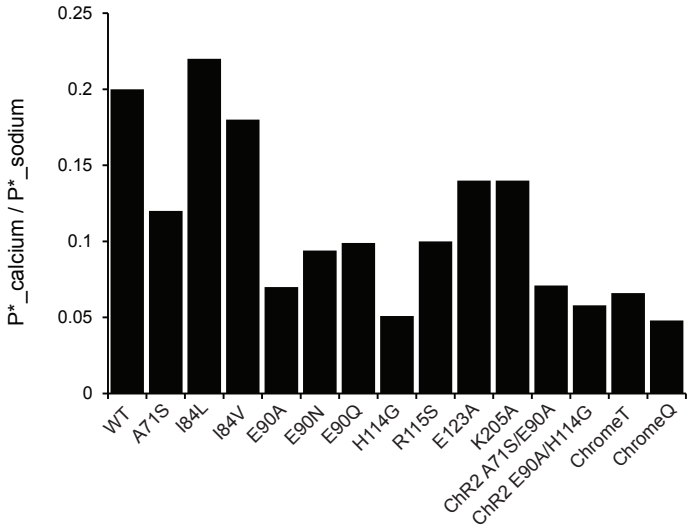

b

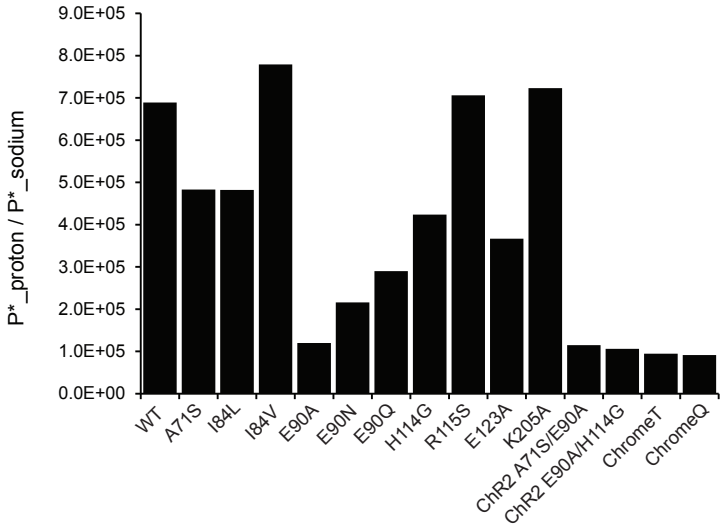

Supplementary Figure-8 (Boyden)

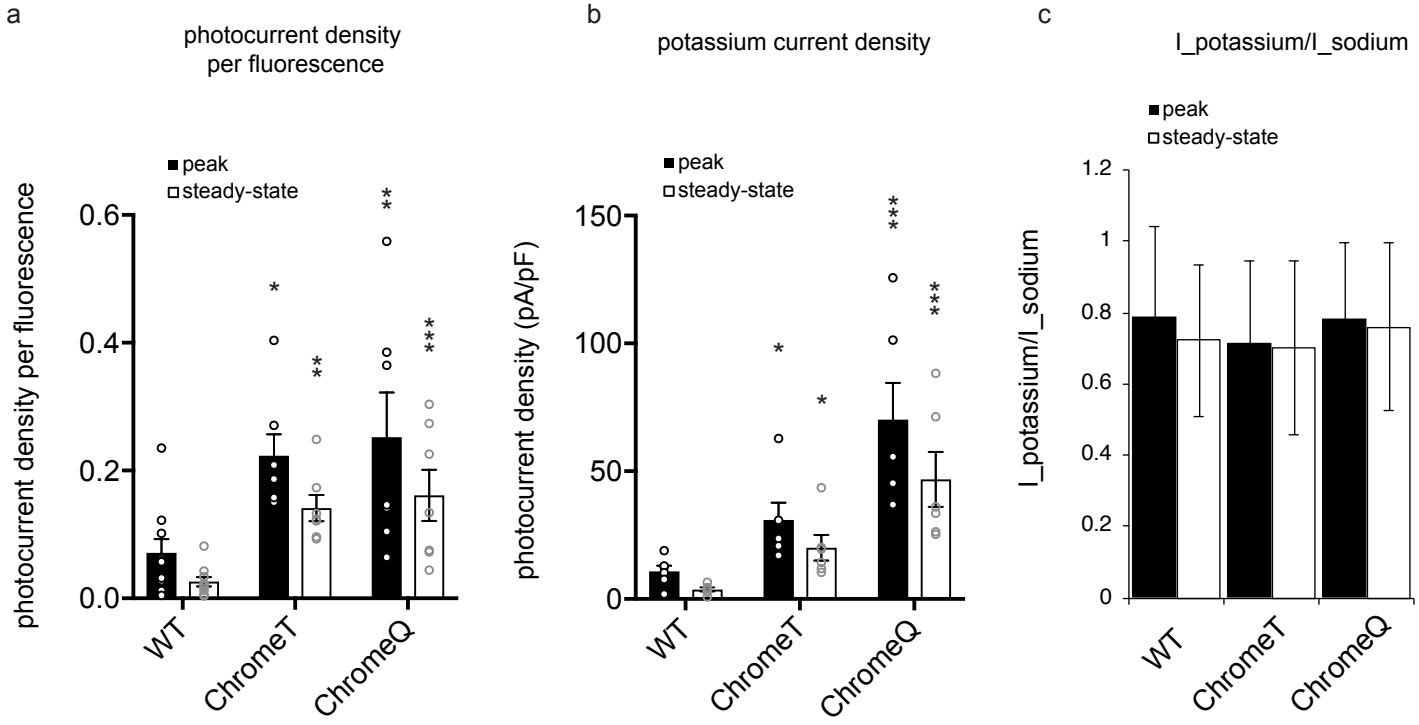

Supplementary Figure-9 (Boyden)

a

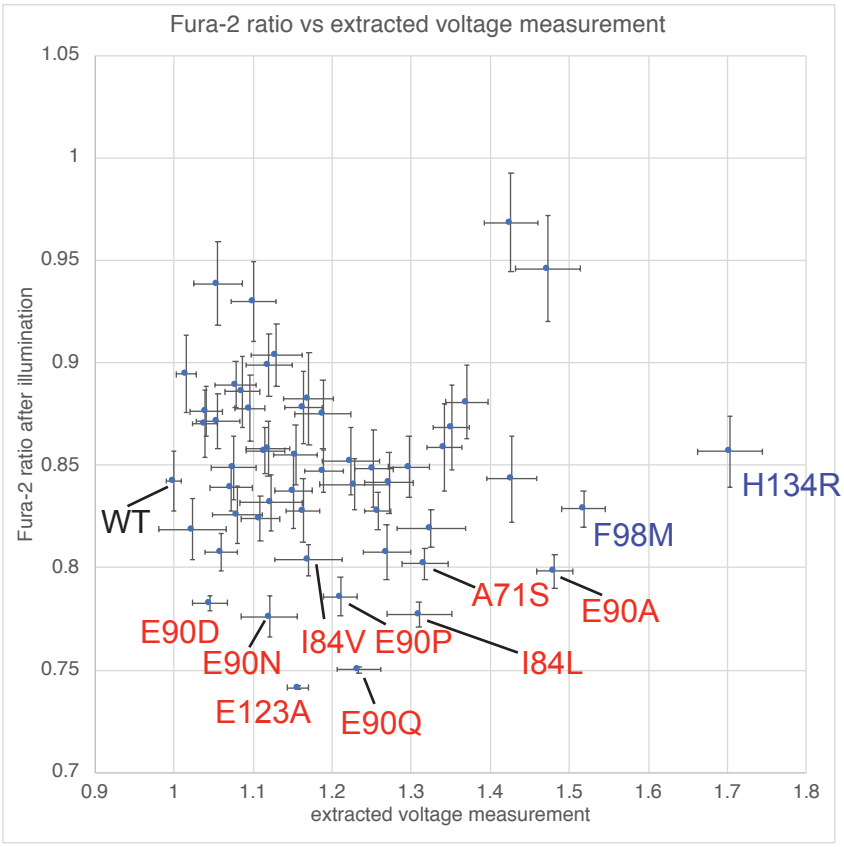

b